IEEE Access
Multidisciplinary ⋮ Rapid Review ⋮ Open Access Journal

Received January 8, 2022, accepted January 16, 2022, date of publication January 19, 2022, date of current version January 28, 2022.

Digital Object Identifier 10.1109/ACCESS.2022.3144669

Constrained Modulated Model Predictive Control for a Three-Phase Three-Level Voltage Source Inverter

JOSUE ANDINO[1,2], (Graduate Student Member, IEEE), PAÚL AYALA[2], (Member, IEEE), JACQUELINE LLANOS-PROAÑO[2], (Member, IEEE), DIEGO NAUNAY[1,2], (Graduate Student Member, IEEE), WILMAR MARTINEZ[3], (Senior Member, IEEE), AND DIEGO ARCOS-AVILES[2], (Senior Member, IEEE)

[1]Maestría de Investigación en Electrónica mención Automática, Universidad de las Fuerzas Armadas ESPE, Sangolquí 171103, Ecuador
[2]Grupo de investigación en Propagación, Control Electrónico y Networking (PROCONET), Departamento de Eléctrica, Electrónica y Telecomunicaciones, Universidad de las Fuerzas Armadas ESPE, Sangolquí 171103, Ecuador
[3]Department of Electrical Engineering, ESAT, KU Leuven-EnergyVille, Diepenbeek, 3600 Genk, Belgium

Corresponding author: Josue Andino (jaandino@espe.edu.ec)

This work was supported in part by the Universidad de las Fuerzas Armadas ESPE and KU Leuven through the Project "MIRA-ESTE: Specific, Innovative Microgrids Solutions (Accounting for Environmental, Social, Technological and Economic Aspects) for isolated rural areas of Ecuador" under Project 2020-EXT-007, and in part by the Vlaamse Interuniversitaire Raad (VLIR)-Universitaire Ontwikkelingssamenwerking (UOS) and the Belgium Development Cooperation (DGD) under Project EC2020SIN322A101.

ABSTRACT In the last decade, model predictive control (MPC) has been widely studied in power converters, such as voltage source inverters (VSIs). Unfortunately, MPC often presents a high computational burden that limits their applicability, especially when driving multilevel inverters (MLIs) because of their higher number of switching combinations than two-level inverters. As a result, some strategies have been developed to reduce the computational complexity of MPC. One of the most relevant is the use of artificial neural networks (ANNs) to approximate the behavior of an MPC. However, ANNs require to be evaluated at bounded inputs. Otherwise, their response cannot be guaranteed to be a good approximation of the controller they learned from. Furthermore, when driving an LC-filtered VSI, the inductor current can present high peaks due to the cross-coupling effect between the inductor and the capacitor. These current peaks can cause physical damages and loss of performance of an ANN-emulated MPC. This paper presents a new constrained modulated MPC (M^2PC), better suited for ANN emulation, to overcome these issues. The proposed strategy evaluates the cost function once per switching region, allowing easy and intuitive constraint inclusion. Additionally, an overmodulation stage is used to handle negative duty cycles and enhance disturbance rejection. Finally, the proposal is validated through simulations, using MATLAB-Simulink, taking into account different load conditions. Simulations show that the constrained M^2PC keeps the inductor current below its desired limit while having a good performance (low harmonic distortions and fast dynamics) even when the inverter operates near its boundaries.

INDEX TERMS DC-AC power converters, modulated model predictive control, multilevel inverter, three-phase inverter.

I. INTRODUCTION

In recent years multi-level inverters (MLIs) have become a vital study focus due to their advantages compared with two-level inverters. MLIs can achieve higher voltages while using lower-voltage switching devices, reducing electromagnetic interference (EMI) due to its lower dv/dt [1]. Moreover, since MLIs produce a staircase output voltage, the resulting total harmonic distortion (THD) is lower, allowing smaller output filters. Furthermore, MLIs reduce the switching losses, which increases the converter efficiency. Consequently, MLIs are becoming more and more popular

The associate editor coordinating the review of this manuscript and approving it for publication was Nagesh Prabhu.

in renewable energy resources, such as solar and wind power [2], [3].

Although MLI topologies are still an open field of research, there are three classical and well-known topologies, such as Cascade H-Bridge, Neutral-Point-Clamped (NPC), and Flying capacitor [2], [4]–[6]. Each of these MLI topologies has its benefits. However, the T-type NPC (T-NPC) has gained a lot of interest recently since it requires fewer switching components and it presents superior thermal and electrical efficiencies than other NPC topologies [7]–[9].

MLI converters benefit from their physical configuration, modulation techniques, and control strategies. On the one hand, there are several modulation techniques, most of them based on the conventional ones, such as Pulse Width Modulation (PWM), Space Vector Modulation (SVM), and Selective Harmonic Elimination (SHE) [1], [10]. Note that SVM brings about a superior performance for T-NPC inverters due to its better use of the DC voltage [11]. For instance, the PWM technique presents a maximum voltage equal to half of the DC-link voltage, (V_{DC}), whereas the SVM technique gives a maximum of $0.577V_{DC}$ [12]. On the other hand, there are numerous control strategies for voltage source inverters (VSIs), namely, sliding mode control (SMC), fuzzy logic control (FLC), PID control, model predictive control (MPC), among others [13]. In this regard, model predictive control (MPC) has been widely studied and developed in the last years, thanks to the ever-increasing computational power of microprocessors [14].

The MPC applied to MLI converters come in two main groups: Finite Control Set MPC (FCS-MPC) and Continuous Control Set MPC (CCS-MPC). The FCS-MPC is the most advanced control strategy thanks to its fast dynamic, multi-objective control, intuitive implementation, and straightforward inclusion of constraints. The FCS-MPC generates a discontinuous control signal to select the optimal switching state among the finite set, making the optimization process easy. Unfortunately, cannot guarantee a fixed switching frequency, increasing the THD and making it harder to filter design and predict switching losses. In contrast, CCS-MPC calculates a continuous control signal which is modulated, usually by a PWM modulator, to drive the converter. The use of the modulator stage keeps fixed the switching frequency which lowers the resulting THD and the switching losses. However, the inclusion of constraints to a CCS-MPC is not an easy task since it requires analytical solutions or the use more complex solvers [15].

Modulated MPC (M^2PC) is a control technique that keeps fixed the switching frequency preserving many benefits of an FCS-MPC. The M^2PC's operating principle applies a set of three optimal switching combinations in a single time interval with their respective duty cycles. Thus, the M^2PC controller produces intermediate switching states, which are not feasible in an FCS-MPC. There are two main alternatives to compute these duty cycles [16]. first, to assume that duty cycles have an inverse relationship with the cost function [8], [16]–[19] and, second, to find the duty cycles based on the deadbeat control theory relationship [16]. Still, the last one can produce duty cycles lower than zero or greater than one without physical meaning. Therefore, the authors in [20], [21] add an optimal overmodulation stage that keeps duty cycles between zero and one. Note that the switching space is usually divided into several switching regions to facilitate the computation of the control law for M^2PC controllers. Each of these regions comprises at least three switching vectors. [19].

The M^2PC controller combines the main advantages of FCS-MPC and CCS-MPC, namely a fast dynamic response at rejecting disturbances of an FCS-MPC and good steady-state performance of a CCS-MPC. Although M^2PC is based on FCS-MPC, adding constraints is not a straightforward task since the M^2PC strategy requires multiple evaluations of the CF per switching region [22], [23]. These multiple evaluations of the CF per switching region can lead to not optimal solutions when constraints are considered, and the system operates near the constraint boundaries. In this scenario, if any of the three switching vectors of a region produces, on its own, a current higher than the maximum allowed, the entire region will be discarded even if the optimal switching vector is also inside the same region. This phenomenon causes a lack of controller performance, such as higher THD.

It is well-known that MPC controllers can lead to computationally complex optimization problems [14], especially for MLI converters, since the amount of possible switching states (SS) is much higher than two-level inverters. There are some proposals to reduce the computational burden of MPC applied to MLIs. For instance, in [24] sorting networks are used to find the optimal control law quickly. However, this strategy still has to evaluate all the considered switching combinations and rank them according to their cost function, so its computation time still depends on the number of levels of an inverter. Other strategies, as in [25], [26] try to reduce the number of possible states by dividing the switching space into several small sectors. This can reduce the controllers' disturbance rejection performance since the control law must be located into one of these small sectors, which is not necessarily the optimal sector.

In recent years, artificial neural networks (ANNs) have been used to reduce the computational burden of MPC controllers. In [27], [28], the behavior of an FCS-MPC has been successfully emulated by using an ANN to classify the next switching state to apply. These approaches demonstrate that an ANN-emulated FCS-MPC can be executed at higher frequencies than a traditional FCS-MPC [28], and it can even make several predictions into the future without increasing the computational burden [27]. However, these approaches have also inherited the previously discussed drawbacks, such as variable switching frequency, of an FCS-MPC. Indeed, these ANN-emulated MPC controllers (ANN-MPC) have, at best, the same behavior as the original controller. Consequently, it is necessary to develop MPC strategies better-suited from ANN emulation (i.e., expert MPC), regardless of their computational complexity.

Although ANNs have excellent performance at recognizing, learning, and generalizing from underlying relationships in a data set, this performance is not ensured when the input lies outside the numerical range used during training [29]. Consequently, ANN-MPC controllers can present poor performances or even instabilities if system variables used to predict the control law lie outside the training range. Therefore, ANN-MPC controllers have to control a system and keep bounded its variables, particularly when external disturbances alter the behavior of the closed-loop system. The authors in [30] mention that robust MPC (RMPC) controllers are suitable for ANN emulation, guaranteeing stability and constraint satisfaction. It is essential to mention that these constraints must be applied not only to the state variables but also to the control law. However, the procedure of developing an RMPC in [30] is hard to extrapolate to other MPC strategies. Guaranteeing constraint satisfaction is usually a challenging task due to the non-linearity nature of the problem [31].

Usually, in LC-filtered VSI, the state variables are the capacitor voltage and the inductor current. In VSIs, the output variable is the capacitor voltage, which is not directly controlled due to the cross-coupling effect between the inductor and the capacitor [32]. The inverter's voltage directly controls the inductor current's gradient, whereas the capacitor's gradient does not. Consequently, high current peaks can be produced if the controller does not limit the inductor current. Thus, limiting the inductor current to an allowed range ensures the safe operation of the hardware and avoids the core saturation of the inductor [15]. Moreover, accomplishing inductor current constraints will result in an ANN-emulable MPC control strategy for LC-filtered VSIs.

To the best of the author's knowledge, there are several reasons why inductor current constraints are not widely used in MPC controllers for power inverters. First, the use of first-order L filters makes adding the inductor current constraint unnecessary, for there is no cross-coupling effect between filter elements [32]. In addition, this approach is used mainly in grid-tied inverters, so the inductor current is already controlled, as in [8], [21], [33]–[35]. Similarly, the current is already controlled when driving induction machines or resistive-inductive loads [20], [36], [37], so there is no need to add current constraints. Second, optimizing a CF in real-time is a time-consuming task. Thus adding constraints to the optimization problem can lead to intractable problems. Moreover, the CF calculation often considers the DC-link voltage balance when driving MLI converters, increasing the number of predictions an MPC must perform [4], [9], [19]. Furthermore, some studies add another constraint to the CF to implement the control law. In [19], the constraints added to ensure that the resulting duty cycles are between zero and one, and that the sum of the three must be equal to one. However, this strategy generates empty areas in the switching space, which increases the resulting THD [38] compared with other M^2PC strategies, such as [20], [21], [39]. However, these studies only consider the sum of the duty cycles as a constrain, and an optimal overmodulation stage is added to handle negative duty cycles. In [40], a combination of FCS-MPC and CCS-MPC is presented, where the CCS-MPC is used for steady-state and the FCS-MPC for the disturbance rejection. Nevertheless, this study only adds an inverter voltage constraint to determine the control law to be applied depending on whether the control law is outside of the switching space or not.

Some studies proved to add current constraints for three-phase inverters successfully. In [36], a current limit is added by scaling the control law or searching for a new one to meet the current constraint. In [41], a new term is added into the CF to remove all the switching states that generate currents higher than the maximum allowed. Although these methods are effective, they are also based on the FCS-MPC. Therefore, they cannot guarantee a fixed switching frequency. Moreover, in [15], a post-correction stage is added to a CCS-MPC controller to limit the inductor current and the inverter voltage. Although it guarantees fixed switching frequency, it requires weighting factors. In addition, the control law constraint is limited to a circle instead of a hexagon, limiting its ability to reject disturbances.

Consequently, ANN-emulated MPC controllers applied to VSIs require learning from MPC controllers with good performance, such as fast dynamic response and low THD at steady-state, regardless of their computational cost. Moreover, these controllers must also guarantee that the system's state variables are bounded, so the ANN will not have to deal with variables outside its training range. Therefore, this study proposes a constrained M^2PC that ensures the inductor current does not exceed a maximum predefined value. The proposed control strategy evaluates the cost function, just once per switching region, at the weighted average of the three voltages of the same region. In addition, an extended overmodulation stage, based on [20], is added to handle negative duty cycles. This overmodulation stage allows the controller to perform faster disturbance rejection. It is important to recall that the proposed strategy is not designed to be executed in real-time but rather to act as an expert controller from which an ANN can learn. The proposed approach could be applied for offline optimization processes.

The main contributions of this study are summarized as follows:

1) Presents an intuitive and straightforward methodology for including constraints into the M^2PC technique.
2) The proposed strategy ensures constraint satisfaction and good closed-loop performance even if the system operates near the constraint boundaries.
3) An extended overmodulation stage is presented to use the entire switching space, ensuring a fast disturbance rejection.

The rest of the paper is organized a follows. Section II describes the mathematical model of the three-phase three-level voltage source inverter (3φ-3L-VSI) with an LC filter. Section III details the three control analyzed in the study,

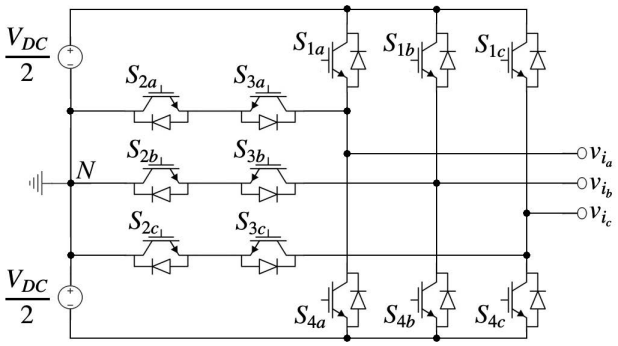

FIGURE 1. Schematic of the 3φ-3L-VSI using the T-NPC topology.

namely, unconstrained M^{2}PC, M^{2}PC with added constraints (which performs multiple evaluations of the cost function), and the proposed constrained M^{2}PC. Simulation results for the three control strategies are presented in Section IV. Finally, Section V presents the main conclusions of this work.

II. SYSTEM MODELING

The converter used in this study consist of an LC-filtered three-phase three-level voltage source inverter (3φ-3L-VSI). This Section presents the mathematical modeling of both inverter and filter using the $\alpha\beta$ transformation (i.e., Clarke transformation). In this regard, all three-phase voltages and currents in the *abc* frame are transformed into $\alpha\beta$ frames by multiplying the *abc* vector times the amplitude invariant Clarke's transformation vector $\mathbf{T}$, as follows:

$$\mathbf{T} = \frac{2}{3}\begin{bmatrix} 1 & e^{j\frac{2}{3}\pi} & e^{j\frac{4}{3}\pi} \end{bmatrix} \tag{1}$$

So that, three-phase voltage vectors $\mathbf{v}_{abc} = [v_a,\ v_b,\ v_c]^T$ and current vectors $\mathbf{i}_{abc} = [i_a,\ i_b,\ i_c]^T$ are represented in the $\alpha\beta$ frame as follows:

$$\begin{aligned} v_{\alpha\beta} &= v_\alpha + jv_\beta = \mathbf{T}\cdot\mathbf{v}_{abc} \\ i_{\alpha\beta} &= i_\alpha + ji_\beta = \mathbf{T}\cdot\mathbf{i}_{abc} \end{aligned} \tag{2}$$

A. THREE-PHASE INVERTER MODEL

The three-phase inverter, shown in Fig. 1, consists of four switching devices (transistors) per leg: S_{1x}, S_{2x}, S_{3x} and S_{4x}, where x $\in \{a, b, c\}$. There are several possible combinations of these switches per leg. However, only three are valid since other states cause short circuits between the DC-link. The switching devices control must take the following considerations into account to avoid short circuits:

- S_{1x} (S_{4x}) and S_{3x} (S_{2x}) must have a complementary operation, which means that if S_{1x} (S_{4x}) is ON, S_{3x} (S_{2x}) must be OFF, and vice-versa.
- S_{1x} and S_{4x} cannot be ON at the same time.
- S_{1x} and S_{4x} can be OFF simultaneously.

Therefore, the s_x switch can take the following states:

$$s_x = \begin{cases} 1 & \text{if } S_{1x} \text{ is ON} \quad \text{and} \quad S_{4x} \text{ is OFF} \\ 0 & \text{if } S_{1x} \text{ is OFF} \quad \text{and} \quad S_{4x} \text{ is OFF} \\ -1 & \text{if } S_{1x} \text{ is OFF} \quad \text{and} \quad S_{4x} \text{ is ON} \end{cases} \tag{3}$$

The inverter output voltages (v_{iaN}, v_{ibN}, and v_{icN}), concerning the DC-link's neutral point N, are obtained by multiplying the half DC-link voltage by the switching state of the corresponding leg (s_a, s_b, and s_c), as follows:

$$\begin{aligned} v_{iaN} &= V_{DC}/2 \cdot s_a \\ v_{ibN} &= V_{DC}/2 \cdot s_b \\ v_{icN} &= V_{DC}/2 \cdot s_c \end{aligned} \tag{4}$$

The effective voltages supplied to the load, i.e., v_{ian}, v_{ibn}, and v_{icn}, are obtained by subtracting the common-mode voltage, v_{nN}, to the inverter output (4), as follows:

$$\begin{aligned} v_{ian} &= v_{iaN} - v_{nN} \\ v_{ibn} &= v_{ibN} - v_{nN} \\ v_{icn} &= v_{icN} - v_{nN} \end{aligned} \tag{5}$$

$$v_{nN} = \frac{v_{iaN} + v_{ibN} + v_{icN}}{3} \tag{6}$$

In $\alpha\beta$ coordinates, the inverter output voltage ($v_{i\alpha\beta}$) is computed as follows:

$$v_{i\alpha\beta} = \mathbf{T}\cdot\begin{bmatrix} v_{ian} \\ v_{ibn} \\ v_{icn} \end{bmatrix} = \frac{V_{DC}}{2}\cdot\mathbf{T}\cdot\left(\mathbf{I} - \frac{1}{3}\mathbf{1}\right)\cdot\mathbf{s} \tag{7}$$

where, $\mathbf{I}$ is the identity matrix, $\mathbf{1}$ is a three-by-three all-ones matrix, and $\mathbf{s}$ is a column vector that represents the commutations of all the three phases (i.e., $\mathbf{s} = [s_a,\ s_b,\ s_c]^T$).

It worth pointing out that $\mathbf{s}$ can take one of the 27 (3^3) possible switching states (SS), where, in the $\alpha\beta$ frame, nineteen states produce non-redundant switching voltages and eight states give redundant voltages. The resulting switching voltages (i.e., switching vectors) are classified into four groups according to their voltage magnitude: zero, small, medium, and large (see Fig. 2 and Table 1). Only zero and small voltages have redundancies since their SS produces equal voltages in the $\alpha\beta$ frame. Note that small voltages control the current flow's direction into the DC-link's neutral point. However, the DC-link dynamics can be decoupled of the inverter dynamics by a proper selection of these redundant SS [34]. Therefore, this study considers a constant DC-link voltage and only the 19 non-redundant SS, listed in Table 1.

In a 3φ-3L-VSI converter, choosing three switching vectors at each sampling time is necessary to implement an SVM algorithm in the M^{2}PC. As mentioned in [19], the switching space can be divided into 24 regions, where each region $\mathcal{R}_j$ (with j $\in \{1, 2, \ldots, 24\}$) comprises three switching voltages ($\mathbf{v_j} = [v_{j1},\ v_{j2},\ v_{j3}]$), being v_{ji} the i-th element of the voltage vector $\mathbf{v_j}$ with i $\in \{1, 2, 3\}$, see Table 2. Consequently, the M^{2}PC control strategy aims to find the optimal region, $\mathcal{R}_{opt}$, at each sampling time k, which contains the optimal voltages to apply, $\mathbf{v_{opt}}$.

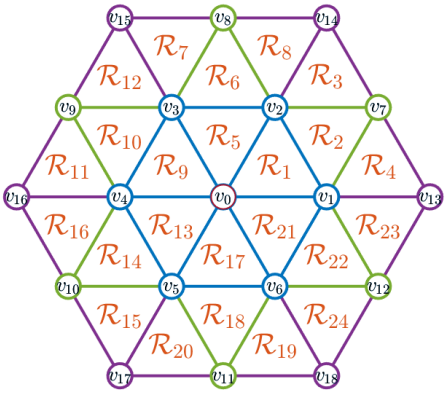

FIGURE 2. Space of switching voltages and regions of the 3φ-3L-VSI: zero voltages v_0, small voltages v_1-v_6, medium voltages v_7-v_{12} and large voltages v_{13}-v_{18}.

TABLE 1. Space of non-redundant switching voltages.

v	s_a	s_b	s_c	$\lvert v_{i\alpha\beta}\rvert/V_{DC}$	$\theta_{v_{i\alpha\beta}}$
v_0	0	0	0	0	0
v_1	0	-1	-1	1/3	0
v_2	1	1	0	1/3	$\pi/3$
v_3	0	1	0	1/3	$2\pi/3$
v_4	-1	0	0	1/3	π
v_5	0	0	1	1/3	$-2\pi/3$
v_6	0	-1	0	1/3	$-\pi/3$
v_7	1	0	-1	$\sqrt{3}/3$	$\pi/6$
v_8	0	1	-1	$\sqrt{3}/3$	$\pi/2$
v_9	-1	1	0	$\sqrt{3}/3$	$5\pi/6$
v_{10}	-1	0	1	$\sqrt{3}/3$	$-5\pi/6$
v_{11}	0	-1	1	$\sqrt{3}/3$	$-\pi/2$
v_{12}	1	-1	0	$\sqrt{3}/3$	$-\pi/6$
v_{13}	1	-1	-1	2/3	0
v_{14}	1	1	-1	2/3	$\pi/3$
v_{15}	-1	1	-1	2/3	$2\pi/3$
v_{16}	-1	1	1	2/3	π
v_{17}	-1	-1	1	2/3	$-2\pi/3$
v_{18}	1	-1	1	2/3	$-\pi/3$

Note. $\lvert v_{i\alpha\beta}\rvert/V_{DC}$ is the magnitude of the inverter voltage concerning the DC-link voltage and $\theta_{v_{i\alpha\beta}}$ is the angle of the inverter voltage in radians.

B. LC FILTER

An *LC* filter is connected to the inverter's output terminals to reduce the harmonic content produced by the switching devices. Each filter leg comprises an inductor L_f, a series resistor R_f, and a parallel capacitor C_f, as shown in Fig. 3. The state-space equation (8) represents the filter dynamics. Note that $i_{f\,\alpha\beta}$ and $v_{f\,\alpha\beta}$ are the state variables of vector $\mathbf{x}_{\alpha\beta}$, whereas $v_{i\alpha\beta}$ and $i_{o\alpha\beta}$ are the system inputs.

$$\dot{\mathbf{x}}_{\alpha\beta} = \frac{d}{dt}\begin{bmatrix} i_{f\,\alpha\beta} \\ v_{f\,\alpha\beta} \end{bmatrix} = \mathbf{A}\cdot\begin{bmatrix} i_{f\,\alpha\beta} \\ v_{f\,\alpha\beta} \end{bmatrix} + \mathbf{B}\cdot\begin{bmatrix} v_{i\alpha\beta} \\ i_{o\alpha\beta} \end{bmatrix}$$

TABLE 2. Voltage distribution for each of the 24 regions in the switching space.

Region ($\mathcal{R}_j$)	Voltage Vector $\mathbf{v_j} = [v_{j1}, v_{j2}, v_{j3}]$
$\mathcal{R}_1$	$\mathbf{v_1} = [v_0\,, v_1\,, v_2]$
$\mathcal{R}_2$	$\mathbf{v_2} = [v_1\,, v_7\,, v_2]$
$\mathcal{R}_3$	$\mathbf{v_3} = [v_2\,, v_7\,, v_{14}]$
$\mathcal{R}_4$	$\mathbf{v_4} = [v_1\,, v_{13}\,, v_7]$
$\mathcal{R}_5$	$\mathbf{v_5} = [v_0\,, v_2\,, v_3]$
$\mathcal{R}_6$	$\mathbf{v_6} = [v_2\,, v_8\,, v_3]$
$\mathcal{R}_7$	$\mathbf{v_7} = [v_3\,, v_8\,, v_{15}]$
$\mathcal{R}_8$	$\mathbf{v_8} = [v_2\,, v_{14}\,, v_8]$
$\mathcal{R}_9$	$\mathbf{v_9} = [v_0\,, v_3\,, v_4]$
$\mathcal{R}_{10}$	$\mathbf{v_{10}} = [v_3\,, v_9\,, v_4]$
$\mathcal{R}_{11}$	$\mathbf{v_{11}} = [v_4\,, v_9\,, v_{16}]$
$\mathcal{R}_{12}$	$\mathbf{v_{12}} = [v_3\,, v_{15}\,, v_9]$
$\mathcal{R}_{13}$	$\mathbf{v_{13}} = [v_0\,, v_4\,, v_5]$
$\mathcal{R}_{14}$	$\mathbf{v_{14}} = [v_4\,, v_{10}\,, v_5]$
$\mathcal{R}_{15}$	$\mathbf{v_{15}} = [v_5\,, v_{10}\,, v_{17}]$
$\mathcal{R}_{16}$	$\mathbf{v_{16}} = [v_4\,, v_{16}\,, v_{10}]$
$\mathcal{R}_{17}$	$\mathbf{v_{17}} = [v_0\,, v_5\,, v_6]$
$\mathcal{R}_{18}$	$\mathbf{v_{18}} = [v_5\,, v_6\,, v_{11}]$
$\mathcal{R}_{19}$	$\mathbf{v_{19}} = [v_6\,, v_{11}\,, v_{18}]$
$\mathcal{R}_{20}$	$\mathbf{v_{20}} = [v_5\,, v_{17}\,, v_{11}]$
$\mathcal{R}_{21}$	$\mathbf{v_{21}} = [v_0\,, v_6\,, v_1]$
$\mathcal{R}_{22}$	$\mathbf{v_{22}} = [v_6\,, v_{12}\,, v_1]$
$\mathcal{R}_{23}$	$\mathbf{v_{23}} = [v_1\,, v_{12}\,, v_{13}]$
$\mathcal{R}_{24}$	$\mathbf{v_{24}} = [v_6\,, v_{18}\,, v_{12}]$

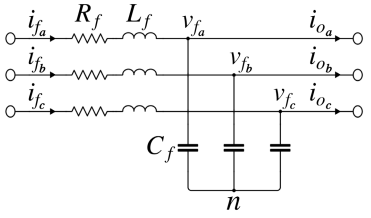

FIGURE 3. Three-phase *LC* filter.

$$\mathbf{A} = \begin{bmatrix} -\frac{R_f}{L_f} & -\frac{1}{L_f} \\ \frac{1}{C_f} & 0 \end{bmatrix}$$
$$\mathbf{B} = \begin{bmatrix} -\frac{1}{L_f} & 0 \\ 0 & \frac{1}{C_f} \end{bmatrix} \tag{8}$$

where $\mathbf{A}$ is the state matrix, $\mathbf{B}$ is the input matrix, $i_{f\,\alpha\beta}$ is the filter current, $v_{f\,\alpha\beta}$ is the filter voltage, $i_{o\alpha\beta}$ is the output current, and $v_{i\alpha\beta}$ is the inverter voltage. All of them in $\alpha\beta$ coordinates.

The prediction of the system's behavior is obtained by discretizing (8) through the zero-order hold (ZOH) for a sampling time T_s as follows:

$$\begin{bmatrix} i_{f\,\alpha\beta,\,k+1} \\ v_{f\,\alpha\beta,\,k+1} \end{bmatrix} = \mathbf{A_d}\begin{bmatrix} i_{f\,\alpha\beta,\,k} \\ v_{f\,\alpha\beta,\,k} \end{bmatrix} + \mathbf{B_d}\begin{bmatrix} v_{i\alpha\beta,\,k} \\ i_{o\alpha\beta,\,k} \end{bmatrix}$$

$$\mathbf{A_d} = e^{\mathbf{A}T_s}$$
$$\mathbf{B_d} = \int_0^{T_s} e^{\mathbf{A}\tau}\mathbf{B}d\tau \tag{9}$$

C. UNIT DELAY COMPENSATION

In general, predictive control algorithms based on FCS-MPC require time to perform their calculations. To compensate this calculation delay, the controller should predict the evolution of the system's behavior, at the time $k+1$, given the already applied control law $v_{i\alpha\beta,\,k}$. Then the controller has to compute, at the time $k+2$, all the possible future behaviors of the inverter voltage v, which will be applied at the time $k+1$. Although the controller can use the output current prediction $i_{o\alpha\beta,\,k+1}$, yhe difference between the present value and the forecast is neglectable (i.e., $i_{o\alpha\beta,\,k+1} \approx i_{o\alpha\beta,\,k}$) when the sampling time, T_s, is much faster than the filter's dynamics. Finally, the controller can compute the $k+2$ predictions using (10), as follows:

$$\begin{bmatrix} i_{f\,\alpha\beta,\,k+2}(v) \\ v_{f\,\alpha\beta,\,k+2}(v) \end{bmatrix} = \mathbf{A_d}\begin{bmatrix} i_{f\,\alpha\beta,\,k+1} \\ v_{f\,\alpha\beta,\,k+1} \end{bmatrix} + \mathbf{B_d}\begin{bmatrix} v \\ i_{o\alpha\beta,\,k} \end{bmatrix} \tag{10}$$

D. CONTROL LAW

As stated in [38], there are several ways to interpret the control law. For instance, as a set of three optimal voltages, $\mathbf{v_{opt}} = [v_{\mathrm{opt}_1},\, v_{\mathrm{opt}_2},\, v_{\mathrm{opt}_3}]$, each one applied with its respective duty cycle, $\mathbf{d} = [d_1,\, d_2,\, d_3]^T$, or as an average complex voltage provided by the inverter, $\bar{v}_{i\alpha\beta}$. The relationship of both approaches is:

$$\bar{v}_{i\alpha\beta} = \mathbf{v_{opt}} \cdot \mathbf{d} \tag{11}$$

III. CONTROL STRATEGY

This Section presents the unconstrained controller and the proposed constrained M^{2}PC. In addition, the CF's multiple evaluations related to constraint inclusion are explained.

A. UNCONSTRAINED M^{2}PC

There are several M^{2}PC implementations, such as [19] and [22]. The M^{2}PC with optimized overshoot strategy was first established for two-level inverters and then extended to 3L-VSI in [20] and [38], respectively. This study uses the M^{2}PC strategy since it makes use of the entire switching space. Even though this strategy is a particular case of the M^{2}PC, it still makes multiple evaluations of the cost function (CF) to determine the optimal switching vectors, so that adding constraints is not straightforward.

The unconstrained M^{2}PC calculates the respective duty cycles of the three active vectors by solving a linear system of equations (12), as follows:

$$\mathbf{V_f(v_{opt})} \cdot \mathbf{d} = \mathbf{v_{ref}} \tag{12}$$

with

$$\mathbf{V_f(v_j)} = \begin{bmatrix} v_{f\,\alpha,k+2}(v_{\mathrm{j}1}) & v_{f\,\alpha,k+2}(v_{\mathrm{j}2}) & v_{f\,\alpha,k+2}(v_{\mathrm{j}3}) \\ v_{f\,\beta,k+2}(v_{\mathrm{j}1}) & v_{f\,\beta,k+2}(v_{\mathrm{j}2}) & v_{f\,\beta,k+2}(v_{\mathrm{j}3}) \\ 1 & 1 & 1 \end{bmatrix} \tag{13}$$

$$\mathbf{v_{ref}} = \begin{bmatrix} v_{ref\,\alpha,\,k+2} \\ v_{ref\,\beta,\,k+2} \\ 1 \end{bmatrix} \tag{14}$$

where $\mathbf{v_j} = [v_{\mathrm{j}1},\, v_{\mathrm{j}2},\, v_{\mathrm{j}3}]$

On the one hand, if the obtained duty cycles are all positive, which means that the filter's voltage is inside the linear modulation zone, these duty cycles are applied the next sampling time. However, although duty cycles are obtained by solving (12), the three switching vectors are chosen by minimizing a CF, with no constraints (15), which quantifies the error between the prediction of the filter's voltage and the prediction of its reference.

$$g(v) = |v_{ref\,\alpha\beta,\,k+2} - v_{f\,\alpha\beta,\,k+2}(v)|^2 \tag{15}$$

Note that $v_{ref\,\alpha\beta,\,k}$ is the reference voltage, which is a sinusoidal signal, and it can be expressed as a complex exponential in $\alpha\beta$ coordinates as in (16) [15], [41].

$$\begin{aligned} v_{ref\,\alpha\beta,\,k} &= v_{ref\,\alpha,\,k} + jv_{ref\,\beta,\,k} \\ &= V_n \cos(2\pi f_n T_s k) + jV_n \sin(2\pi f_n T_s k) \\ &= V_n \exp(j2\pi f_n T_s k) \end{aligned} \tag{16}$$

where, V_n is the nominal voltage amplitude, f_n the nominal frequency, and T_s is the sampling time.

In addition, as stated in [19], the switching vectors can be grouped in regions. Therefore, it is better to find the optimal region, $\mathcal{R}_{\mathrm{opt}}$, containing the optimal switching vectors, $\mathbf{v_{opt}}$. In this regard, (17) defines a cost function for the regions as the sum of the cost of the regions' three switching vectors, as follows:

$$G_{\mathrm{j}} = \sum_{\mathrm{i}=1}^{3} g(v_{\mathrm{ji}}) \tag{17}$$

Therefore, the optimal region, $\mathcal{R}_{\mathrm{opt}}$, is obtained by minimizing (17):

$$\mathcal{R}_{\mathrm{opt}} = \arg\min_{\mathrm{j}} G_{\mathrm{j}} \tag{18}$$

On the other hand, it is possible to obtain negative duty cycles after solving the linear system in (12). The SVM modulator cannot implement these duty cycles since they lack physical meaning. However, they indicate to the controller that the reference is outside the selected switching region (i.e., the controller cannot reach the reference value in one sampling time), and it requires the application of an overmodulation strategy. If null and small voltages (v_0-v_6) are always in the first position of the voltage vector $\mathbf{v_j}$, only the first duty cycle (d_1) can be negative since these voltages are the only ones able to produce negative duty cycles (see Table 2).

The angles θ and ϕ should be calculated using (19) to perform the overmodulation algorithm.

$$\theta = \arccos\left(\frac{\Re\mathfrak{e}\{x_1 x_3^*\}}{|x_1||x_3|}\right) \tag{19a}$$

$$\phi = \arccos\left(-\frac{\Re\{x_2 x_3^*\}}{|x_2||x_3|}\right) \tag{19b}$$

with

$$\begin{aligned} x_1 &= v_{ref\,\alpha\beta,\,k+2} - v_{f\,\alpha\beta,\,k+2}(v_{\text{opt}_2}) \\ x_2 &= v_{ref\,\alpha\beta,\,k+2} - v_{f\,\alpha\beta,\,k+2}(v_{\text{opt}_3}) \\ x_3 &= v_{f\,\alpha\beta,\,k+2}(v_{\text{opt}_2}) - v_{f\,\alpha\beta,\,k+2}(v_{\text{opt}_3}) \end{aligned} \tag{20}$$

Knowing the angles θ and ϕ, the new duty cycles applied in the next sampling time, are calculated as follows:

$$\mathbf{d} = \begin{bmatrix} 0 & d_\phi & d_\theta \end{bmatrix}^T \tag{21}$$

with

$$d_\phi = \begin{cases} \dfrac{|x_2|}{|x_3|}\cos\phi & \text{if } \theta, \phi < \pi/2 \\ 1 & \text{if } \phi \geq \pi/2 \\ 0 & \text{otherwise} \end{cases} \tag{22}$$

$$d_\theta = \begin{cases} \dfrac{|x_1|}{|x_3|}\cos\theta & \text{if } \theta, \phi < \pi/2 \\ 1 & \text{if } \theta \geq \pi/2 \\ 0 & \text{otherwise} \end{cases} \tag{23}$$

Fig. 4 shows the flowchart for implementing the unconstrained M^{2}PC control strategy.

B. M^{2}PC WITH CONTRAINTS

The term h_{lim} is included for adding the current constraint into the CF [41], consequently discarding all possible switching combinations that produce an inductor current higher than the desired maximum, $I_{f_{max}}$, so that the constrained cost function g_c is defined as follows:

$$g_c(v) = g(v) + h_{lim}(i_{f\,\alpha\beta,\,k+2}(v)) \tag{24}$$

with

$$h_{lim}(i_{f\,\alpha\beta}) = \begin{cases} 0 & \text{if } |i_{f\,\alpha\beta}| < I_{f_{max}} \\ \infty & \text{if } |i_{f\,\alpha\beta}| \geq I_{f_{max}} \end{cases} \tag{25}$$

Even though the strategy described in Section III-A is potent and easy to use, it does not support the addition of constraints in the cost function since the method requires the cost function evaluation at the three switching vectors that form a region to find the optimal region $\mathcal{R}_{\text{opt}}$ (i.e., $G_{\text{j}} = \sum_{v\in\mathcal{R}_{\text{j}}} g_c(v) = g_c(v_{\text{j}1}) + g_c(v_{\text{j}2}) + g_c(v_{\text{j}3})$). Therefore, if one of the voltages, on its own, makes the inductor current surpass the maximum value, $I_{f_{max}}$, the whole region should be discarded even if the resulting current meets the constraint after applying the linear combination of these three switching vectors (11).

For instance, suppose the switching space in Fig. 5. As it can be seen the optimal region is $\mathcal{R}_{\text{opt}} = \mathcal{R}_8$, so that the optimal voltages are $\mathbf{v_{opt}} = \mathbf{v_8} = [v_2,\ v_{14},\ v_8]$. In addition, the inductor constraint, $I_{f_{max}}$, divides the optimal region into two areas, green and red. Suppose the prediction of the current, $i_{f\,\alpha\beta,\,k+2}$, represented by the blue arrow, lies inside the green area. In that case, $\mathcal{R}_8$ should be accepted as the optimal region since a linear combination of its voltages will not produce a current higher than $I_{f_{max}}$. Conversely, if the prediction lies in the red area, it should be discarded, and the optimization process will have to move to another region.

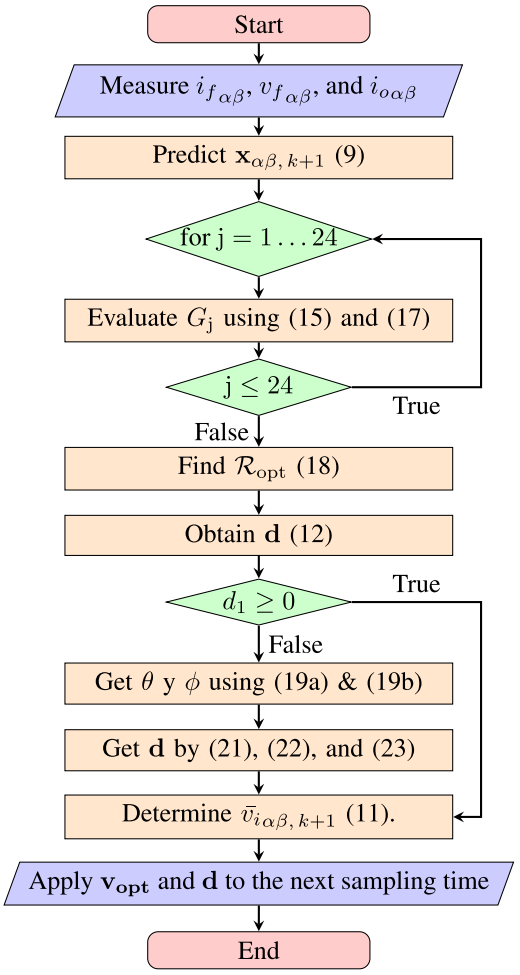

FIGURE 4. Unconstrained M^{2}PC flow chart.

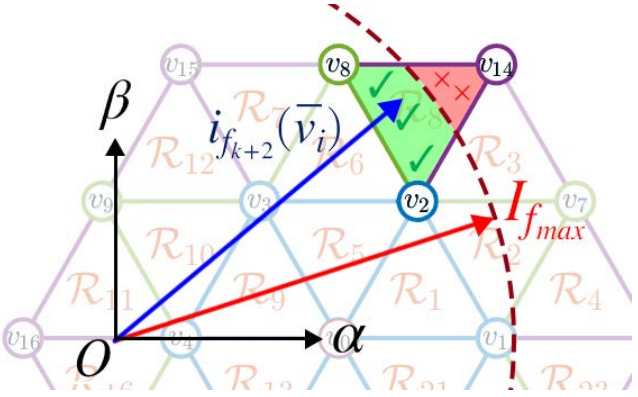

FIGURE 5. Illustration of the multiple evaluation of the cost function when constraints are added. Blue arrow represents the prediction of the current, red dashed line is the current constraint, red area is prohibited since produces currents higher than the maximum allowed, whereas green area produces valid currents.

Suppose the algorithm, described in Section III-A, is used to determine the optimal region in Fig. 5. In that case, it will mark the region as not valid since its cost function will have an infinite value even though the resulting current after applying these voltages will not surpass the current constraint $I_{f_{max}}$. That is:

$$G_8 = g_c(v_2) + \cancelto{\infty}{g_c(v_{14})} + g_c(v_8) = \infty \tag{26}$$

Multiple evaluations of the CF per region can lead to not optimal solutions, which can negatively impact the controller performance, especially at disturbance rejection when the controller produces higher voltages. Consequently, the system is more likely to surpass its constraints.

C. PROPOSED CONSTRAINED M^{2}PC

In order to include constraints to the M^{2}PC control strategy and to not worsen the performance of the strategy described in III-B, the following modifications are proposed:

1) COST FUNCTION EVALUATION

The CF is evaluated at the three voltages of each region to determine the optimal region value since each voltage contributes to the resulting evolution of the system's behavior. Therefore, after selecting a region, $\mathcal{R}_\text{j}$, the predicted state of the system, $\bar{\mathbf{x}}_{\alpha\beta,\,k+2,\text{j}}$, in that region can be determined as the weighted average of the system's behavior predictions $\mathbf{x}_{\alpha\beta,\,k+2}$ evaluated on each voltage v_ji in the region:

$$\begin{aligned}\bar{\mathbf{x}}_{\alpha\beta,\,k+2,\text{j}} = {} & d_1\mathbf{x}_{\alpha\beta,\,k+2}(v_{\text{j}1}) \\ & + d_2\mathbf{x}_{\alpha\beta,\,k+2}(v_{\text{j}2}) + d_3\mathbf{x}_{\alpha\beta,\,k+2}(v_{\text{j}3})\end{aligned} \tag{27}$$

Since $d_1 + d_2 + d_3 = 1$ and the LC filter is a linear system, the system's predicted state is computed as follows:

$$\begin{aligned}\bar{\mathbf{x}}_{\alpha\beta,\,k+2,\text{j}} &= \mathbf{x}_{\alpha\beta,\,k+2}(d_1v_{\text{j}1} + d_2v_{\text{j}2} + d_3v_{\text{j}3}) \\ &= \mathbf{x}_{\alpha\beta,\,k+2}(\mathbf{v_j}\cdot\mathbf{d}) \\ &= \mathbf{x}_{\alpha\beta,\,k+2}(\bar{v}_\text{j})\end{aligned} \tag{28}$$

In short, the system's predicted state, at time $k+2$, can be obtained by evaluating (10) at the weighted average voltage $\bar{v}_\text{j}$ the *j-th* region can produce, with $\bar{v}_\text{j} = \mathbf{v_j}\cdot\mathbf{d}$. Therefore, the CF evaluation uses the weighted average voltage instead of the three voltages of a region:

$$\bar{G}_\text{j} = g_c(\bar{v}_\text{j}) \tag{29}$$

Therefore, the optimal region $\mathcal{R}_\text{opt}$, which contains the control law applied to the following sampling time, is the one that minimizes $\bar{G}_\text{j}$:

$$\mathcal{R}_\text{opt} = \arg\min_\text{j} \bar{G}_\text{j} \tag{30}$$

2) EXTENDED OVERMODULATION STAGE

The constraints added to the M^{2}PC strategy bring about an undesired phenomenon named Internal Overmodultaion (IOM). The difference between the IOM and the traditional overmodulation, called External Overmodulation (EOM), is where these phenomena occur. As its name implies, EOM occurs at the external edges of the switching space, whereas IOM at the internals, as shown in Fig. 6.

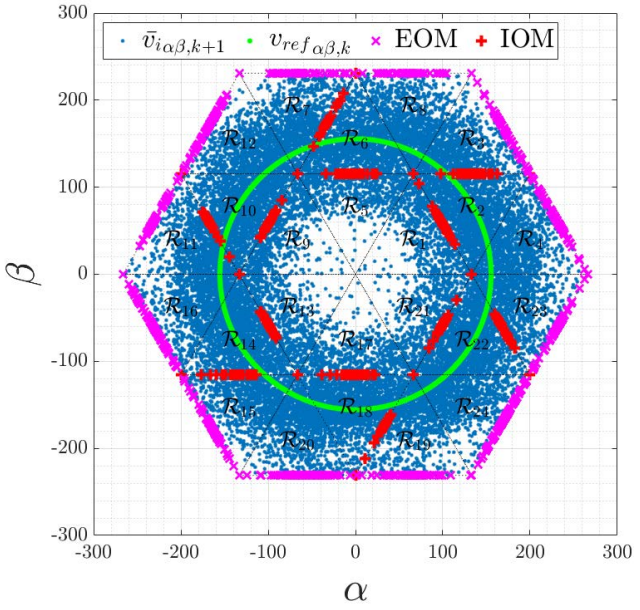

FIGURE 6. Control law (blue dots) and reference voltage (green line) on the switching space. Points where EOM and IOM ocurr are highlighted with magenta and red colors, respectively.

Section III-A states that to determine whether the control law needs to be overmodulated or not, the first duty cycle d_1 must be compared with zero. If it is lower, the overmodulation algorithm must be applied. However, this detection method only works with EOM, for null and small voltages are the only ones that can produce a negative duty cycle in this scenario. In contrast, when IOM occurs, any of the three elements of $\mathbf{d}$ can produce a negative duty cycle. Note that the duty cycles are calculated first by solving the linear system of equations for each region in the switching space, i.e., $\mathbf{V_f(v_j)}\cdot\mathbf{d} = \mathbf{v_{ref}}$. After that, overmodulation must be applied if any duty cycles are negative.

The proposed modification is to calculate x_1, x_2 and x_3 first depending on which duty cycle is negative (31) so that the control strategy can still compute the angles θ and ϕ using (19), as follows:

$$\begin{aligned}x_1 &= v_{ref\,\alpha\beta,\,k+2} - v_{f\,\alpha\beta,\,k+2}(u) \\ x_2 &= v_{ref\,\alpha\beta,\,k+2} - v_{f\,\alpha\beta,\,k+2}(w) \\ x_3 &= v_{f\,\alpha\beta,\,k+2}(w) - v_{f\,\alpha\beta,\,k+2}(u)\end{aligned} \tag{31}$$

with

$$u = \begin{cases} v_{\text{j}2} & \text{if } d_1 < 0 \\ v_{\text{j}1} & \text{if } d_2 < 0 \\ v_{\text{j}1} & \text{if } d_3 < 0 \end{cases} \tag{32}$$

$$w = \begin{cases} v_{\text{j}3} & \text{if } d_1 < 0 \\ v_{\text{j}3} & \text{if } d_2 < 0 \\ v_{\text{j}2} & \text{if } d_3 < 0 \end{cases} \tag{33}$$

TABLE 3. Simulation Parameters.

	Parameter	Value	Unit
V_{DC}	DC-link voltage	400	V
V_n	Nominal phase voltage	156	V
f_n	Nominal frequency	60	Hz
T_s	Sampling time	100	μs
f_{sw}	SVM frequency	10	kHz
L_f	Filter inductance	2.4	mH
C_f	Filter capacitance	24	μF
R_f	Filter resistance	0.1	Ω
R	Resistive load	11	Ω
C_n	Nonlinear load capacitance	110	μF
R_n	Nonlinear load resistance	26	Ω

Finally, the new duty cycles are calculated by using (22) and (23). These new duty cycles are placed as follows:

$$\mathbf{d} = \begin{cases} \begin{bmatrix} 0 & d_\phi & d_\theta \end{bmatrix}^T & \text{if } d_1 < 0 \\ \begin{bmatrix} d_\phi & 0 & d_\theta \end{bmatrix}^T & \text{if } d_2 < 0 \\ \begin{bmatrix} d_\phi & d_\theta & 0 \end{bmatrix}^T & \text{if } d_3 < 0 \end{cases} \tag{34}$$

The flow chart of the proposed constrained M^{2}PC control strategy is shown in Fig 7. The main difference with the flow chart in Fig. 4 is that duty cycles are calculated for all the 24 regions, including solving the linear system in (12) and applying the extended overmodulation stage when needed. Note that since all the 24 regions have their own set of voltages and duty cycles, the optimal ones are found by minimizing (30).

IV. SIMULATION AND RESULTS

A. SIMULATION SETUP

The control loop, shown in Fig. 8, is simulated in Matlab®-Simulink to validate the proposed control strategy. Table 3 presents the simulation parameters used in this study. For comparison purposes, this study compares three control strategies previously described, namely the unconstrained M^{2}PC (Section III-A), used as a reference [20], the M^{2}PC with constraints added to its cost function using the h_{lim} term described in [41] (Section III-B), and the proposed constrained M^{2}PC (Section III-C). In addition, an unconstrained FCS-MPC and a constrained FCS-MPC are used as a baseline performance. Note that these two controllers are not developed in this work, for they are already well-known. Moreover, the comparison is performed using three different loads: a resistive load, a nonlinear load (see Fig. 9), and a no-load at the inverter's output. Three criteria are selected, namely, total harmonic distortion (THD), steady-state error (SSE), and settling time (t_s) to evaluate the performance of each controller under these loads. Additionally, the inductor current constraint is $I_{f_{max}}$ = 15 A.

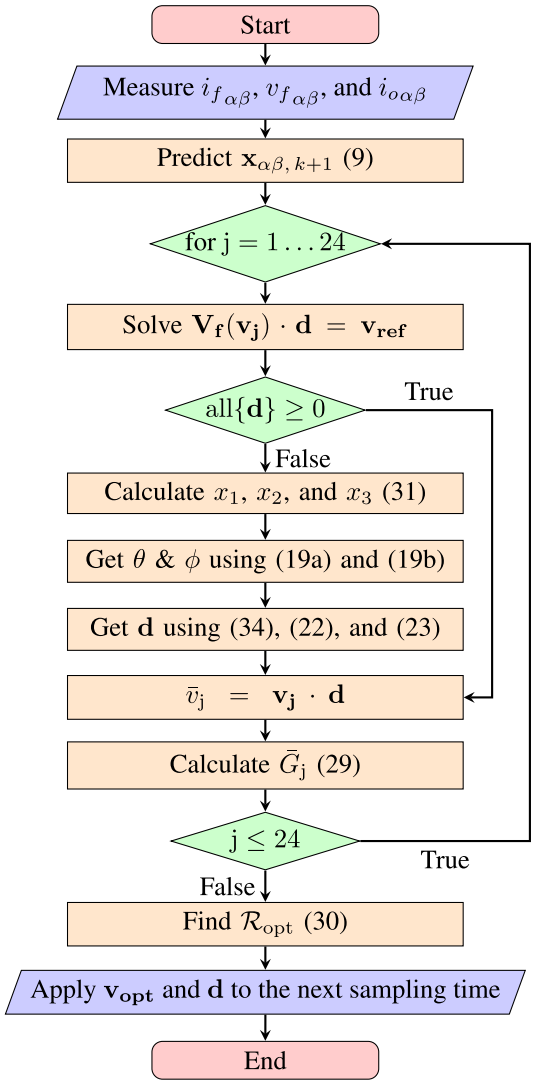

FIGURE 7. Proposed constrained M^{2}PC flow chart.

B. SIMULATION RESULTS

Fig. 10, Fig. 11, and Fig. 12 show the dynamic behavior of the three strategies for a linear load, nonlinear load, and no-load, respectively, connected to the inverter output. These figures on the top present the filter voltages $v_{f\alpha}$, $v_{f\beta}$ (solid blue line and solid orange line, respectively), and the reference voltage $v_{ref\,\alpha\beta}$ (black dashed line), whereas, at the bottom, they show the magnitude of the filter's current $|i_{f\,\alpha\beta}|$ (solid green line) and the current constraint $I_{f_{max}}$ (red dotted line). Finally, blue dashed ellipses and magenta dashed rectangles highlight the regions of interest. Note that there is a time window, t_s, limited by the black dotted vertical lines, where the disturbance is not yet rejected.

Fig. 10 shows the dynamic behavior of the three strategies when a resistive load of $R = 11\Omega$ is connected to the inverter's output. The unconstrained M^{2}PC requires 0.9 *ms* (see Fig. 10(a) top) to reject the load disturbance, whereas the proposed constrained M^{2}PC needs 0.8 *ms* (see Fig. 10(c) top). Note that the M^{2}PC with constraints does not reach a

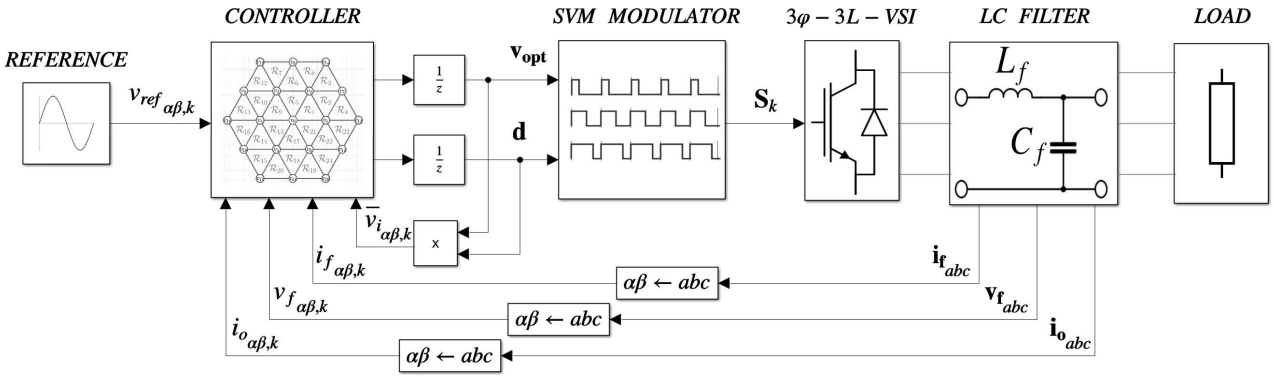

FIGURE 8. Control loop scheme of the 3φ-3L-VSI.

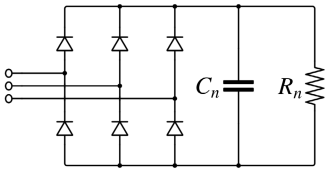

FIGURE 9. Nonlinear load: three-phase diode-bridge rectifier in parallel with a RC branch.

steady-state. The slight difference between the unconstrained M^{2}PC and the proposed one is that the unconstrained M^{2}PC produces a current peak of 18 A (see blue ellipse on Fig. 10(a) bottom). This current propagates into the capacitor voltage due to the cross-coupling effect. In contrast, the proposed constrained M^{2}PC does not produce any current peak (see blue ellipse on Fig. 10(c) bottom). Moreover, at steady-state, both the unconstrained and the proposed constrained M^{2}PC produce stable inductor currents with a ripple of approximately ± 0.5 A, where none of these fluctuations reach the current limit (see magenta rectangle on Fig. 10(a) and Fig. 10(c) bottom). Note that the inductor current for the unconstrained M^{2}PC is slightly smoother than the proposed constrained M^{2}PC since constraints force the controller to make more transitions between regions in the switching space. This behavior causes a negligible higher THD (approximately 0.01%) and makes the current ripple appear noisier than the unconstrained M^{2}PC since the control law directly influences the current. On the contrary, the fluctuations of the M^{2}PC with constraints continually hit the current condition (see magenta rectangle on Fig. 10(b) bottom).

The resulting performance criteria values, of the three controllers, when driving a linear load, are summarized in Table 4. It is worth pointing out that the performance criteria of the proposed constrained M^{2}PC present an improvement regarding the M^{2}PC with constraints. As aforementioned, the behavior of the proposed constrained M^{2}PC is similar to the unconstrained M^{2}PC's performance at steady-state.

The improved behavior of the proposed constrained controller is highlighted when driving nonlinear loads, such as rectifiers that usually contain capacitors that require the charging of high currents. Fig. 11 shows the dynamic behavior of the three strategies when a nonlinear load is connected to the inverter's output. The unconstrained M^{2}PC requires 10 *ms* to reject the disturbance (see Fig. 11(a) top), whereas the proposed constrained M^{2}PC needs 12.5 *ms* (see Fig. 11(c) top). As expected, the M^{2}PC with constraints does not reach a steady-state in this scenario. Moreover, the settling time of the unconstrained M^{2}PC is lower than the proposed constrained M^{2}PC since the unconstrained one is capable of delivering higher currents to the load (see blue ellipse at the bottom of Fig. 11(a) and Fig. 11(c)). However, in steady-state, the resulting currents of these two strategies are similar. Note that none of them reach the limit (see magenta rectangle at the bottom of Fig. 11(a) and Fig. 11(c)). In contrast, the resulting currents of the M^{2}PC with constraints reach the limit regularly (see magenta rectangle at the bottom of Fig. 11(b)) since to keep the current away from its constraint, the M^{2}PC with constraints controller reduces the inductor current, deviating the output voltage. Therefore, the controller must increase the inductor current to compensate for the voltage deviation. The performance criteria of the three controllers when a nonlinear load is connected to the inverter output are summarized in Table 5.

The performance of the three modulated controllers is similar when analyzing the last scenario (see Fig. 12) when no-load is connected to the inverter's output. This behavior

TABLE 4. Performance criteria when a resistive load is connected to the inverter's output.

Controller	THD(%)	SSE(%)	$t_s(ms)$
Unconstrained FCS-MPC	6.58	6.26	-
Constrained FCS-MPC	6.63	10.13	-
Unconstrained M^{2}PC	0.15	2.67	0.9
M^{2}PC w/ Constraints	6.03	10.73	-
Proposed Constrained M^{2}PC	0.16	2.67	0.8

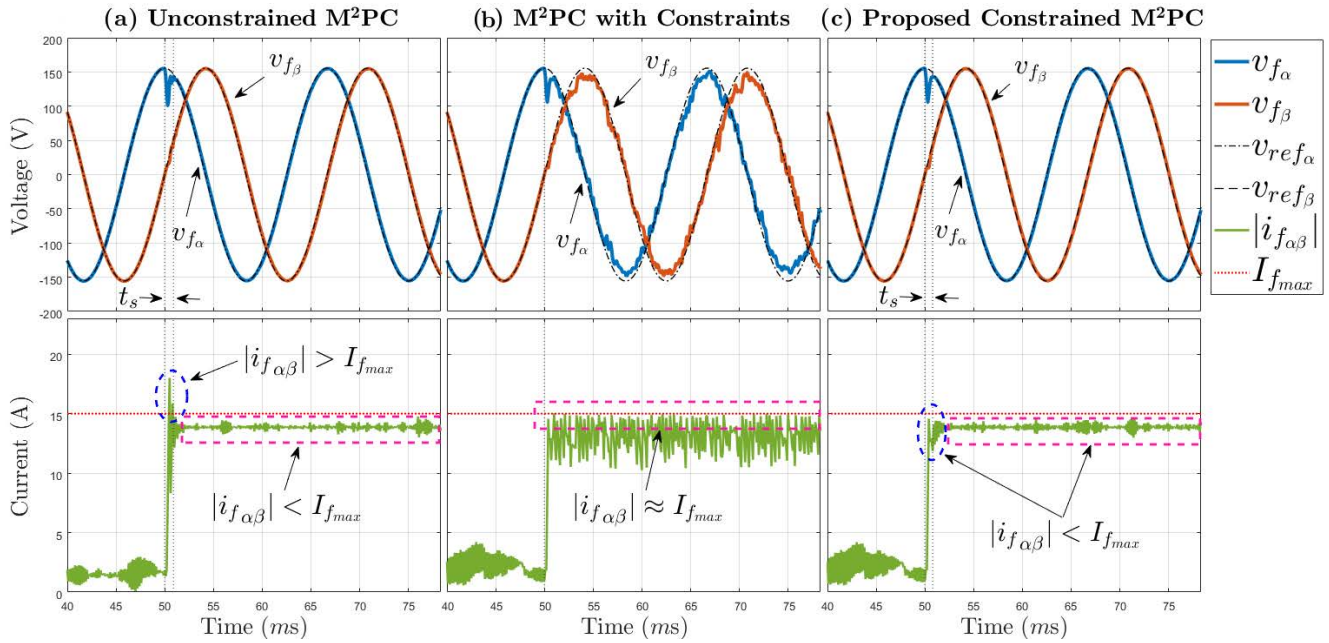

FIGURE 10. Simulation performance, when a linear load is connected at 50 ms, (a) the unconstrained M²PC, (b) an M²PC with added constraints, and (c) the proposed constrained M²PC.

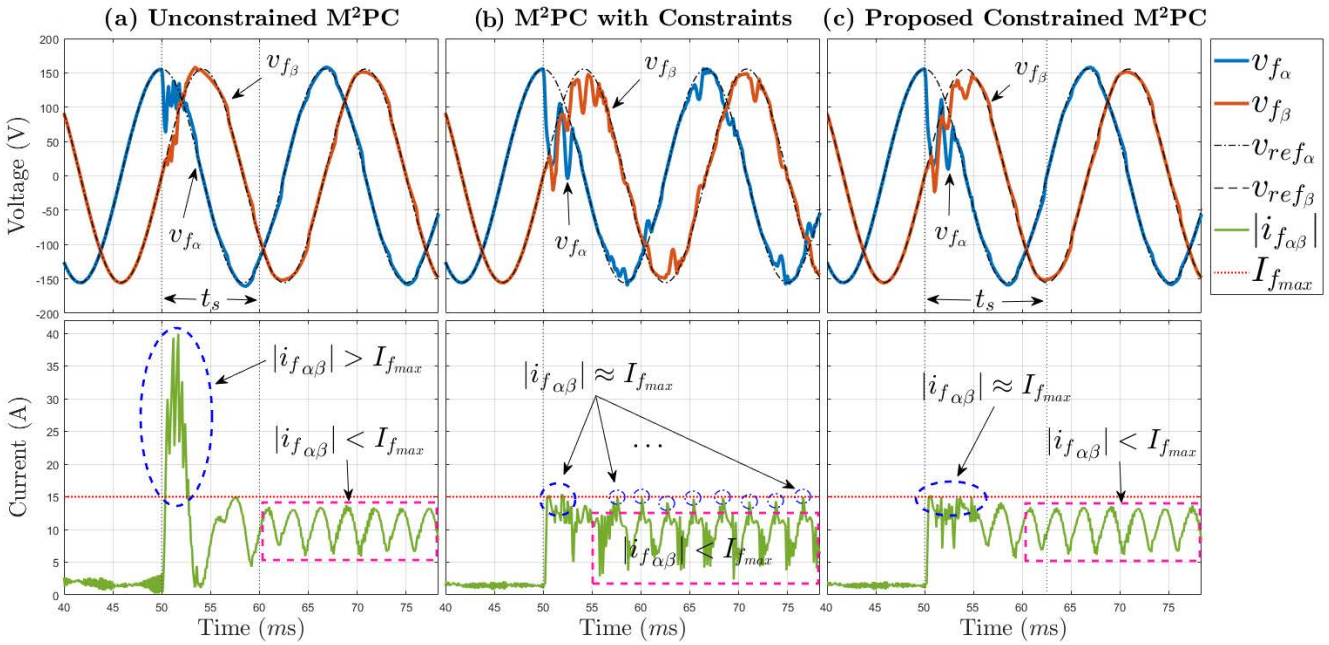

FIGURE 11. Simulation performance, when a nonlinear load is connected at 50 ms, (a) the unconstrained M²PC, (b) an M²PC with added constraints, and (c) the proposed constrained M²PC.

is since the inductor current is far away from its limit almost all the time (i.e., $|i_{f_{\alpha\beta}}| < I_{f_{max}}$). Therefore, the current constraint is always satisfied. However, it should be pointed out that there is a slight difference between Fig. 12(a) compared with Fig. 12(b) and Fig. 12(c) due to the current constraint. In the beginning, the unconstrained M²PC shows a current peak of 23 A (see the bottom of Fig. 12(a)), which is not shown in the other two strategies (see the bottom of Fig. 12(a) and Fig. 12(c)). The current peak achieved by unconstrained M²PC makes the system reach steady-state faster (1 *ms*) regarding the other two strategies (1.4 *ms*). Finally, Table 6 presents the archived performance criteria values for the three analyzed controllers in this scenario.

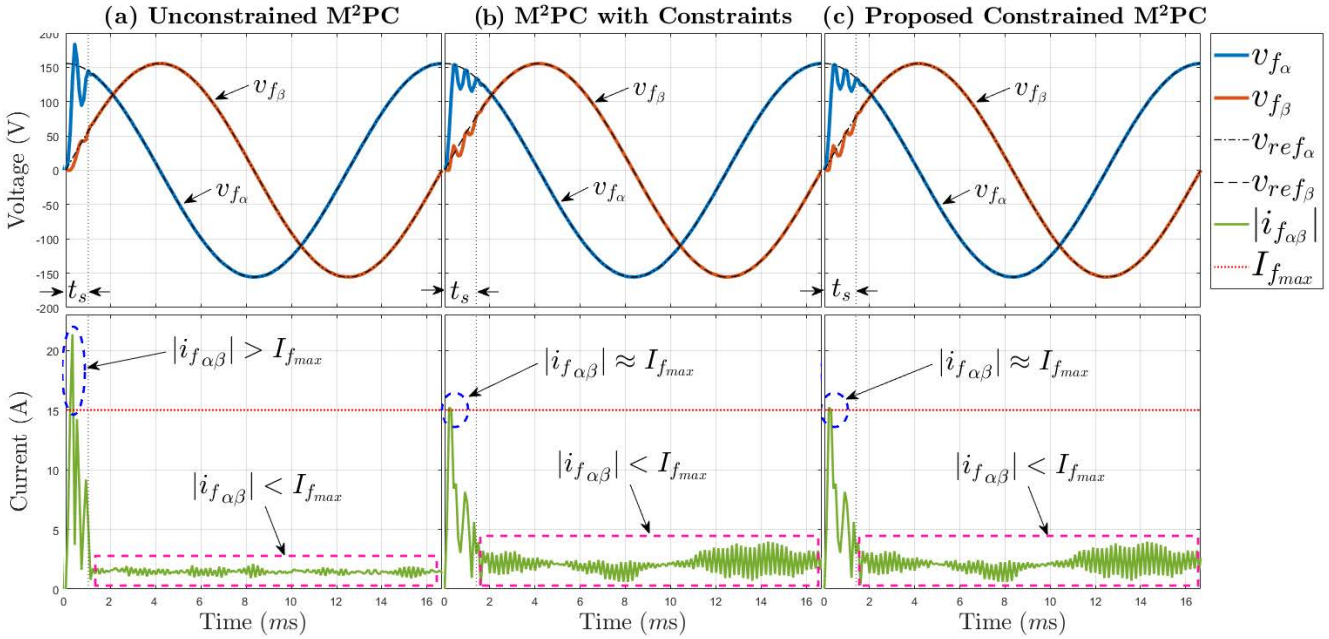

FIGURE 12. Simulation performance, when no-load is connected to the inverter's output, (a) the unconstrained M²PC, (b) an M²PC with added constraints, and (c) the proposed constrained M²PC.

TABLE 5. Performance criteria when a nonlinear load is connected to the inverter's output.

Controller	THD(%)	SSE(%)	$t_s(ms)$
Unconstrained FCS-MPC	7.59	8.65	-
Constrained FCS-MPC	8.51	10.20	-
Unconstrained M²PC	3.50	3.30	10
M²PC w/ Constraints	9.46	8.46	-
Proposed Constrained M²PC	3.51	3.31	12.5

TABLE 6. Performance criteria when a no-load is connected to the inverter's output.

Controller	THD(%)	SSE(%)	$t_s(ms)$
Unconstrained FCS-MPC	6.01	5.92	-
Constrained FCS-MPC	6.25	5.57	-
Unconstrained M²PC	0.16	0.15	1
M²PC w/ Constraints	0.17	0.15	1.4
Proposed Constrained M²PC	0.17	0.15	1.4

C. SENSITIVITY ANALYSIS

A variation of the filter parameters, inductance (ΔL_f) and capacitance (ΔC_f), within $\pm 30\%$ of their nominal values (see Table 3) is made to analyze the robustness of the proposed controller including uncertainties. The THD is selected as a performance criterion. For the sake of simplicity, one parameter is varied at a time, and a resistive load is chosen in this analysis.

Fig. 13(a) shows the influence of inductance uncertainties on the resulting THD. On the one hand, if the controllers overestimate the inductance value (i.e., the filter inductance is lower than its nominal value, $\Delta L_f < 10\%$), the resulting THD abruptly increases. This increment is due to faster inductor dynamics than the controllers expect, for the rate of change of the inductor current depends on the inverse of the inductance (8). It can be noticed that the unconstrained M²PC produces the highest THD, whereas the other two controllers have a similar performance. The constraints inclusion causes this difference since it reduces current filter peaks and, as a result, reduces voltage deviations. On the other hand, if the controller underestimates the inductance (i.e., the filter inductance is higher than its nominal value, $\Delta L_f > 0\%$), the resulting THD slowly increases for all the controllers. In this scenario, the current filter dynamics are slower than expected. In addition, the unconstrained M²PC presents an improved performance than the other controllers since constraint inclusion unnecessarily limits the inductor current regularly, deviating the output voltage. Lastly, the unconstrained M²PC and the proposed constrained M²PC have the lowest THD when the filter inductance is close to its nominal value (i.e., $\Delta L_f \approx 0\%$). Therefore, the predictive model is accurate, and the proposed constrained M²PC has a better constraint handling than the M²PC with constraints.

Conversely, the resulting THD barely changes when a capacitance uncertainty exists, as shown in Fig. 13(b). This dependence on the capacitance is due to slower filter voltage dynamics than current filter dynamics. In addition, the voltage filter is indirectly controlled by the inverter voltage due to the cross-coupling effect between the inductor

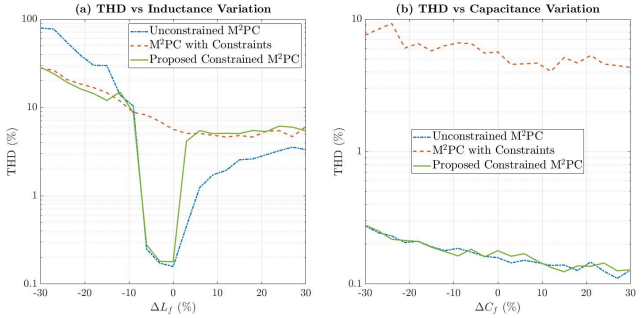

FIGURE 13. Sensitivity analysis of the unconstrained M^{2}PC (blue dash-doted line), M^{2}PC with constraints (orange dashed line), and the proposed constrained M^{2}PC (green solid line). (a) Inductance variation (ΔL_f); (b) Capacitance variation (ΔC_f).

and capacitor. Thus, inductance uncertainties are more critical than capacitance uncertainties. Lastly, the resulting THD of the M^{2}PC with constraints is, as expected, higher than the proposed M^{2}PC and the unconstrained M^{2}PC.

D. COMPUTATIONAL BURDEN

Although the proposed control strategy is designed to be emulated by an ANN, its calculation burden is discussed in this section. It is worth noting that the computational burden of the M^{2}PC with constraints is similar to the unconstrained M^{2}PC since they differ only in including restrictions. Therefore, only the computational burden of the unconstrained M^{2}PC and the proposed constrained M^{2}PC are discussed. The computational complexity of the controllers under test can be divided into four different calculations: system state predictions, cost function evaluation, duty cycle calculation, and optimization.

Each analyzed control strategy must perform twenty predictions of the state variables, nineteen for the $k+2$ predictions, and one for the unit-delay compensation. In addition, each control strategy must also obtain the optimal region by finding the minimal cost function value, which is evaluated at each of the 24 regions. The unconstrained M^{2}PC only requires nineteen evaluations of the cost function, expressed in (15), to obtain the cost of the 24 regions (17). In contrast, the proposed constrained M^{2}PC requires evaluating its cost function (29) once per region.

Moreover, duty cycles are the most time-consuming calculation since they require solving the three-by-three linear system (12) and applying nonlinear functions (19) when needed. The unconstrained M^{2}PC only has to find the duty cycle once per sampling time. In contrast, the proposed constrained M^{2}PC has to perform these calculations one per region per sampling time, which increases the computational burden of the proposed strategy. Simulation results show that the proposal requires 4.5 times than the unconstrained M^{2}PC needs. However, it is worth recalling that the proposed strategy is not designed to be implemented directly but rather emulated by offline training an ANN with higher execution speeds.

V. CONCLUSION AND FUTURE WORK

This paper has developed a novel constrained M^{2}PC strategy for an LC-filtered 3φ-3L-VSI converter. The proposed strategy has been designed to act as an expert controller from which an ANN can learn. In this regard, the proposed controller has focused on limiting the filter current to guarantee the response of an ANN when having bounded inputs. The proposed strategy has evaluated the cost function once per switching region, allowing constraints to be included easily. Moreover, an extended overmodulation stage has been added to enhance disturbance rejection and maintain duty cycles between zero and one. The proposed constrained M^{2}PC has been tested in Matlab-Simulink under three different loads and compared with an unconstrained M^{2}PC and an M^{2}PC with added constraints. Simulation results have demonstrated the effectiveness of the proposed constrained M2PC strategy. The proposed controller has maintained the magnitude of the inductor current below a predefined limit in all the scenarios. In contrast, the unconstrained M2PC has evidenced current peaks over the limit. Furthermore, the proposed M^{2}PC has improved steady-state performance than M^{2}PC with constraints in all the scenarios. Finally, the proposed constrained M^{2}PC has demonstrated keeping the inductor current bounded and excellent steady-state performance.

Future work will focus on approximating the behavior of the proposed constrained M^{2}PC by using an ANN. In addition, experimental results will be presented and validated in practical applications.

REFERENCES

[1] A. Poorfakhraei, M. Narimani, and A. Emadi, "A review of modulation and control techniques for multilevel inverters in traction applications," *IEEE Access*, vol. 9, pp. 24187–24204, 2021.

[2] M. Vijeh, M. Rezanejad, E. Samadaei, and K. Bertilsson, "A general review of multilevel inverters based on main submodules: Structural point of view," *IEEE Trans. Power Electron.*, vol. 34, no. 10, pp. 9479–9502, Oct. 2019.

[3] S. P. Sunddararaj and S. S. Rangarajan, "An extensive review of multilevel inverters based on their multifaceted structural configuration, triggering methods and applications," *Electronics*, vol. 9, no. 3, p. 433, Mar. 2020.

[4] A. R. Kumar and T. Deepa, "Multilevel inverters: A review of recent topologies and new modulation techniques," in *Proc. Int. Conf. Recent Trends Electr., Control Commun. (RTECC)*, Mar. 2018, pp. 196–203.

[5] V. Aishwarya and K. G. Sheela, "Review of reduced-switch multilevel inverters for electric vehicle applications," *Int. J. Circuit Theory Appl.*, vol. 49, no. 9, pp. 3053–3110, Jun. 2021.

[6] M. Trabelsi, H. Vahedi, and H. Abu-Rub, "Review on single-DC-source multilevel inverters: Topologies, challenges, industrial applications, and recommendations," *IEEE Open J. Ind. Electron. Soc.*, vol. 2, pp. 112–127, Jan. 2021.

[7] J. Loncarski, V. G. Monopoli, R. Leuzzi, L. Risti, and F. Cupertino, "Analytical and simulation fair comparison of three level Si IGBT based NPC topologies and two level SiC MOSFET based topology for high speed drives," *Energies*, vol. 12, p. 4571, Nov. 2019.

[8] Y. Yang, H. Wen, M. Fan, M. Xie, R. Chen, and Y. Wang, "A constant switching frequency model predictive control without weighting factors for T-type single-phase three-level inverters," *IEEE Trans. Ind. Electron.*, vol. 66, no. 7, pp. 5153–5164, Jul. 2019.

[9] J. Xu, T. B. Soeiro, F. Gao, H. Tang, and P. Bauer, "A simplified modulated model predictive control for a grid-tied three-level T-type inverter," in *Proc. IEEE 29th Int. Symp. Ind. Electron. (ISIE)*, Jun. 2020, pp. 618–623.

[10] J. I. Leon, S. Kouro, L. G. Franquelo, J. Rodriguez, and B. Wu, "The essential role and the continuous evolution of modulation techniques for voltage-source inverters in the past, present, and future power electronics," *IEEE Trans. Ind. Electron.*, vol. 63, no. 5, pp. 2688–2701, May 2016.
[11] M. Sajitha, J. Sandeep, and R. Ramchand, "Comparative analysis of different modulation techniques for three level three phase T-type NPC inverter," in *Proc. TENCON IEEE Region Conf. (TENCON)*, Oct. 2019, pp. 1529–1534.
[12] K. G. Krishna, T. K. Kumar, and P. V. Rao, "Better DC bus utilization and torque ripple reduction by using SVPWM for VSI fed induction motor drive," *Int. J. Comput. Electr. Eng.*, vol. 4, no. 2, pp. 202–206, Apr. 2012.
[13] S. Tahir, J. Wang, M. Baloch, and G. Kaloi, "Digital control techniques based on voltage source inverters in renewable energy applications: A review," *Electronics*, vol. 7, no. 2, p. 18, Feb. 2018.
[14] P. Karamanakos, E. Liegmann, T. Geyer, and R. Kennel, "Model predictive control of power electronic systems: Methods, results, and challenges," *IEEE Open J. Ind. Appl.*, vol. 1, pp. 95–114, 2020.
[15] C. Zheng, T. Dragičević, B. Majmunović, and F. Blaabjerg, "Constrained modulated model-predictive control of an LC-filtered voltage-source converter," *IEEE Trans. Power Electron.*, vol. 35, no. 2, pp. 1967–1977, Feb. 2020.
[16] L. Cao, Y. Li, X. Li, L. Guo, N. Jin, and H. Cao, "A dual-vector modulated model predictive control method for voltage source inverters with a new duty cycle calculation method," *Energies*, vol. 13, no. 16, p. 4200, Aug. 2020.
[17] P. Santis, D. Sáez, R. Cárdenas, and A. Núñez, "Pareto-based modulated model predictive control strategy for power converter applications," *Electr. Power Syst. Res.*, vol. 171, pp. 158–174, Jun. 2019.
[18] L. Tarisciotti, J. Lei, A. Formentini, A. Trentin, P. Zanchetta, P. Wheeler, and M. Rivera, "Modulated predictive control for indirect matrix converter," *IEEE Trans. Ind. Appl.*, vol. 53, no. 5, pp. 4644–4654, Sep./Oct. 2017.
[19] F. Donoso, A. Mora, R. Cárdenas, A. Angulo, D. Sáez, and M. Rivera, "Finite-set model-predictive control strategies for a 3L-NPC inverter operating with fixed switching frequency," *IEEE Trans. Ind. Electron.*, vol. 65, no. 5, pp. 3954–3965, May 2018.
[20] C. F. Garcia, C. A. Silva, J. R. Rodriguez, P. Zanchetta, and S. A. Odhano, "Modulated model-predictive control with optimized overmodulation," *IEEE J. Emerg. Sel. Topics Power Electron.*, vol. 7, no. 1, pp. 404–413, Mar. 2019.
[21] A. Sarajian, C. F. Garcia, Q. Guan, P. Wheeler, D. A. Khaburi, R. Kennel, J. Rodriguez, and M. Abdelrahem, "Overmodulation methods for modulated model predictive control and space vector modulation," *IEEE Trans. Power Electron.*, vol. 36, no. 4, pp. 4549–4559, Apr. 2021.
[22] H.-J. Yoo, T.-T. Nguyen, and H.-M. Kim, "MPC with constant switching frequency for inverter-based distributed generations in microgrid using gradient descent," *Energies*, vol. 12, no. 6, p. 1156, Mar. 2019.
[23] F. Sebaaly, H. Vahedi, H. Y. Kanaan, and K. Al-Haddad, "Novel current controller based on MPC with fixed switching frequency operation for a grid-tied inverter," *IEEE Trans. Ind. Electron.*, vol. 65, no. 8, pp. 6198–6205, Aug. 2018.
[24] K. Bandy and P. Stumpf, "Model predictive torque control for multilevel inverter fed induction machines using sorting networks," *IEEE Access*, vol. 9, pp. 13800–13813, 2021.
[25] Q. Wang, H. Yu, C. Li, X. Lang, S. S. Yeoh, T. Yang, M. Rivera, S. Bozhko, and P. Wheeler, "A low-complexity optimal switching time-modulated model-predictive control for PMSM with three-level NPC converter," *IEEE Trans. Transport. Electrific.*, vol. 6, no. 3, pp. 1188–1198, Sep. 2020.
[26] Y. Yang, H. Wen, M. Fan, L. He, M. Xie, R. Chen, M. Norambuena, and J. Rodriguez, "Multiple-Voltage-Vector model predictive control with reduced complexity for multilevel inverters," *IEEE Trans. Transport. Electrific.*, vol. 6, no. 1, pp. 105–117, Mar. 2020.
[27] M. Novak and T. Dragicevic, "Supervised imitation learning of finite-set model predictive control systems for power electronics," *IEEE Trans. Ind. Electron.*, vol. 68, no. 2, pp. 1717–1723, Feb. 2021.
[28] I. S. Mohamed, S. Rovetta, T. D. Do, T. Dragicevic, and A. A. Diab, "A neural-network-based model predictive control of three-phase inverter with an output LC Filter," *IEEE Access*, vol. 7, pp. 124737–124749, 2019.
[29] A. Trask, F. Hill, S. Reed, J. Rae, C. Dyer, and P. Blunsom, "Neural arithmetic logic units," in *Proc. Adv. Neural Inf. Process. Syst.*, 2018, pp. 8035–8044.
[30] M. Hertneck, J. Kohler, S. Trimpe, and F. Allgower, "Learning an approximate model predictive controller with guarantees," *IEEE Control Syst. Lett.*, vol. 2, no. 3, pp. 543–548, Jul. 2018.
[31] M. Zanon and S. Gros, "Safe reinforcement learning using robust MPC," *IEEE Trans. Autom. Control*, vol. 66, no. 8, pp. 3638–3652, Aug. 2021.
[32] C. Zheng, T. Dragicevic, Z. Zhang, J. Rodriguez, and F. Blaabjerg, "Model predictive control of LC-filtered voltage source inverters with optimal switching sequence," *IEEE Trans. Power Electron.*, vol. 36, no. 3, pp. 3422–3436, Mar. 2021.
[33] M. R. Chowdhury, S. Chowdhury, M. A. Rahman, and M. R. Islam, "Advanced switching sequences based model-predictive control for single-phase NPC converters," *IEEE Trans. Ind. Electron.*, vol. 69, no. 4, pp. 3515–3526, Apr. 2022.
[34] S. R. Mohapatra and V. Agarwal, "Model predictive controller with reduced complexity for grid-tied multilevel inverters," *IEEE Trans. Ind. Electron.*, vol. 66, no. 11, pp. 8851–8855, Nov. 2019.
[35] M.-V. Doi, B.-X. Nguyen, and N.-V. Nguyen, "A finite set model predictive current control for three-level NPC inverter with reducing switching state combination," in *Proc. IEEE 4th Int. Future Energy Electron. Conf. (IFEEC)*, Nov. 2019, pp. 1–9.
[36] J. Zou, W. Xu, J. Zhu, and Y. Liu, "Low-complexity finite control set model predictive control with current limit for linear induction machines," *IEEE Trans. Ind. Electron.*, vol. 65, no. 12, pp. 9243–9254, Dec. 2018.
[37] F. Toso, P. G. Carlet, A. Favato, and S. Bolognani, "On-line continuous control set MPC for PMSM drives current loops at high sampling rate using qpOASES," in *Proc. IEEE Energy Convers. Congr. Expo. (ECCE)*, Sep. 2019, pp. 6615–6620.
[38] A. B. Josue, P. Ayala, J. Llanos, D. Naunay, W. Martinez, and D. Arcos-Aviles, "Comparison of two modulated model predictive control strategies applied to a three-level three-phase voltage source inverter," in *Proc. IECON 47th Annu. Conf. IEEE Ind. Electron. Soc.*, Oct. 2021, pp. 1–7.
[39] A. Mora, R. Cárdenas-Dobson, R. P. Aguilera, A. Angulo, F. Donoso, and J. Rodriguez, "Computationally efficient cascaded optimal switching sequence MPC for grid-connected three-level NPC converters," *IEEE Trans. Power Electron.*, vol. 34, no. 12, pp. 12464–12475, Mar. 2019.
[40] H. T. Nguyen and J.-W. Jung, "Disturbance-rejection-based model predictive control: Flexible-mode design with a modulator for three-phase inverters," *IEEE Trans. Ind. Electron.*, vol. 65, no. 4, pp. 2893–2903, Apr. 2018.
[41] T. Dragičević, "Model predictive control of power converters for robust and fast operation of AC microgrids," *IEEE Trans. Power Electron.*, vol. 33, no. 7, pp. 6304–6317, Jul. 2018.

JOSUE ANDINO (Graduate Student Member, IEEE) was born in Quito, Ecuador, in 1992. He received the B.Sc. degree in electronics, automation and control engineering and the Electronic Research Master's Degree Automatic Mention from the Universidad de las Fuerzas Armadas ESPE, Sangolquí, Ecuador, in 2015 and 2021, respectively.

He is an Active Member of the Research Group of Propagation, Electronic Control, and Networking (PROCONET), Universidad de las Fuerzas Armadas ESPE. His research interests include power electronics, renewable energies, control systems, and artificial intelligence.

PAÚL AYALA (Member, IEEE) was born in Quito, Ecuador, in 1974. He received the B.E. and M.B.A. degrees in electronics, automation, and control engineering from Armed Forces University–ESPE, Ecuador, in 1997 and 2002, respectively, the M.S. degree in mechatronics from the Universitat Politècnica de Catalunya, Barcelona, Spain, in 2004, and the Ph.D. degree in technical science in the automation and control from the Universidad Tecnológica de la Habana (CUJAE).

Since 1998, he has been a Full Professor with the Department of Electrical, Electronics, and Telecommunications Engineering, Universidad de las Fuerzas Armadas ESPE. His research interests include energy efficiency, advanced control systems, and power electronics.

JACQUELINE LLANOS-PROAÑO (Member, IEEE) received the B.Sc. and Engineering degrees in electronic engineering from the Army Polytechnic School, Ecuador, and the M.Sc. and Ph.D. degrees in electrical engineering from the University of Chile, Santiago. She is currently an Assistant Professor with the Department of Electrical and Electronics, Universidad de las Fuerzas Armadas ESPE, Ecuador. Her current research interests include control and management of microgrids, control of power generation plants, and predictive control.

DIEGO NAUNAY (Graduate Student Member, IEEE) was born in Quito, Ecuador, in 1991. He received the B.Sc. degree in mechatronics engineering from the Universidad de las Fuerzas Armadas ESPE, Ecuador, in 2015, where he is currently pursuing the M.Sc. degree in electronics.

He is part of the Research Group of Propagation, Electronic Control, and Networking (PROCONET), Universidad de las Fuerzas Armadas ESPE. His current research interests include power electronics, predictive control, and control of power electronics.

WILMAR MARTINEZ (Senior Member, IEEE) received the M.Sc. degree in electrical engineering from the Universidad Nacional de Colombia, in 2013, and the Ph.D. degree in power electronics from Shimane University, Japan, in 2016. He was a Postdoctoral Researcher at the Toyota Technological Institute, Japan, in 2016, and at Aalto University, Finland, in 2017. In 2018, he was a Visiting Researcher with the Power Electronic Systems (PES) Group, ETH Zurich, Switzerland. Since 2018, he has been an Assistant Professor with the Department of Electrical Engineering (ESAT), KU Leuven-EnergyVille, Belgium. His current research interests include design automation of power converters, evaluation of iron losses in magnetic materials, and the study of wide bandgap switches for electric mobility, renewable energy systems, and for smart grids.

DIEGO ARCOS-AVILES (Senior Member, IEEE) was born in Quito, Ecuador, in 1978. He received the B.Sc. degree in electronics, automation and control engineering from the Universidad de las Fuerzas Armadas ESPE, Sangolquí, Ecuador, in 2002, and the M.Sc. and Ph.D. degrees in electronics engineering from the Universitat Politècnica de Catalunya, Barcelona, Spain, in 2012 and 2016, respectively.

He has been an Associate Professor with the Department of Electrical, Electronics, and Telecommunications Engineering, Universidad de las Fuerzas Armadas ESPE, since 2002. He is the Editor-in-Chief of *Maskay* journal. Since 2017, he has been the Co-ordinator of the Research Group of Propagation, Electronics Control, and Networking (PROCONET). He has been the Co-ordinator of the master's degree program in electronics, since 2019. He has been involved in many research projects related to microgrids, power electronics, automation of industrial processes, control systems applications, and control of power electronics. His research interests include energy management systems, microgrids, power electronics, smart grids, and renewable generation systems.